Langmuir

ARTICLE

pubs.acs.org/Langmuir

Mimicking Natural Fibrous Structures of Opals by Means of a Microemulsion-Mediated Hydrothermal Method

Natalia Hassan,[‡] Valeria Verdinelli,[†] Juan M. Ruso,[‡] and Paula V. Messina*[,†]

[†]INQUISUR-CONICET, Department of Chemistry, Universidad Nacional del Sur, (8000) Bahía Blanca, Argentina

[‡]Soft Matter and Molecular Biophysics Group, Department of Applied Physics, University of Santiago de Compostela, Santiago de Compostela, 15782, Spain

Supporting Information

ABSTRACT: Silica-based nanomaterials are of great interest because of their potential applications in constructing electronic and optoelectronic nanodevices. Especially significant are those that combine the properties of photonic crystal with a fibrous semiconductor structure. Here we report the use of microemulsion droplet systems as a simple and controllable route for the synthesis of 3D opals materials with an unusual fibrous microstructure similar to those that exist in nature. By this method, we demonstrate the creation of very long fibrils of 30−50 nm diameter and more than 20 μm length showing simultaneous short and long wavelength light emissions and band gap values (5.50 and 4.41 eV) comparable to those obtained for silicon-based metal oxide semiconductors.

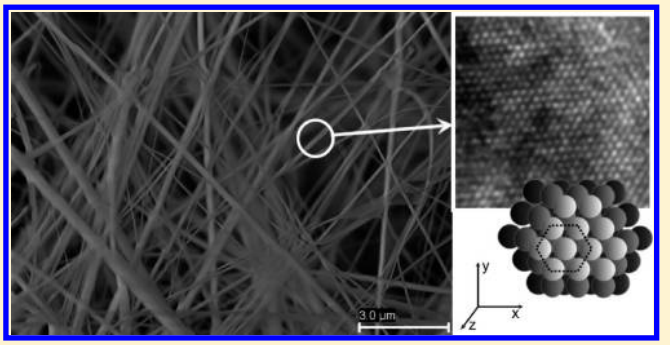

INTRODUCTION

Silicon-based fiber devices are the backbone of modern optoelectronic[1−8] and telecommunication[9,10] systems and are widely used for guiding and distributing light in optical arrangements.[11] A novel type of optical fiber developed mainly during the past decade and pioneered by Russell[12] and co-workers is the microstructured fiber, frequently called the photonic crystal fiber (PCF). PCFs are fibers with an internal periodic structure made of capillaries, filled with air, laid to form a hexagonal lattice. The capillary stack-and-draw procedure proved to be highly versatile, allowing the construction of complex lattices to be assembled from individual stackable units of the correct size and shape. Functional defects can be precisely introduced during the stacking process, allowing fabrication of a wide range of different PCFs.[12]

Opals were identified as natural photonic crystals (PCs) in 1995,[13] and thereafter there have been numerous reports on their structural and optical properties because of their ability to manipulate the flow of light. Most reference describes them as a perfect stacking of amorphous, hydrous silica spheres of identical diameter ranging from 150 to 300 nm.[6,7,14] Nevertheless, in extreme and specific geological conditions they crystallize in the unusual form of nanometer-scale fibrils.[15] Accordingly, one might think of these types of natural opals as photonic crystal nanofibers.

In this paper, we take a significant step toward generating PCFs in a nanometric scale similar to those that exist in nature. For this purpose, we show a bottom-up reverse microemulsion-based method[16] to control the stacking morphology and growth of the opal crystals. The formation and the morphological control of colloidal assemblies during a microemulsion-mediated hydrothermal synthesis is a complex process which depends on the particular combination of all the relevant microemulsion parameters. The effect of various factors on the final particle size is actually system specific, including the rate and the order of reactants addition.[16] Crystalline oxide nanorods can be prepared directly by alkoxide hydrolysis in microemulsions at room temperature. To illustrate, γ-V_2O_5 nanorods of the orthorhombic structure were obtained by direct hydrolysis of a vanadium alkoxide in sodium bis-(2-ethylhexyl) sulfosuccinate (so-called "Aerosol-OT", abbreviated as AOT) reverse micelles,[17] while rodlike ZnO nanoparticles of the hexagonal wurtzite structure were produced by the ammonia-catalyzed hydrolysis of zinc dibutoxide in nonionic reversed micelles.[18] Particularly, the microemulsion-mediated hydrothermal method has been shown to be useful in the synthesis of a variety of 1-D nanostructures. Single-crystalline nanowires/nanorods of CdS,[19] BaF_2,[20] SnO_2,[21] $AlPO_4$-5,[22,23] and $Ca_{10}(PO_4)_6(OH)_2$[24] have been successfully obtained by reverse micelles under hydrothermal conditions.

Here, the microemulsion was treated as a pseudoternary system with oil, water, and surfactant components. The effects of microemulsion oil phase, the hydrothermal treatment time,

Received: February 8, 2011
Revised: May 26, 2011
Published: June 14, 2011

dx.doi.org/10.1021/la201555f | *Langmuir* 2011, 27, 8905–8912

and the calcination temperature on the final material structure were investigated. Thus, two different materials constituted by opal microstructured fibrils were created by sodium tetraethyl orthosilicate hydrolysis inside water/AOT/*n*-hexane and water/AOT/cyclohexane nanodroplets after 24 h of hydrothermal treatment at 100 °C and 7 h of calcination at 650 °C in an air flux. Depending of the microemulsion template system, they showed simultaneous short and long wavelength light emissions and band gap values comparable to those obtained for silicon-based metal oxide semiconductors (MOS). In general, the combination of a fibrous structure and photonic crystal proterties just with a semiconductor structure provides to the PCFs a series of unique properties impossible to achieve in classical silicon fibers. For example: PCFs maximize nonlinear interactions between laser light and low-density media such as gases; in PCFs small dielectric particles can be trapped, levitated, or propelled in a laser beam using the dipole forces exerted by light; and PCFs with extremely small solid glass cores and very high air-filling fractions not only display unusual chromatic dispersion but also yield very high optical intensities per unit power.[1,9,12]

The reduction of such materials at the nanometer scale offers a number of outstanding optical and mechanical properties, including (1) large evanescent fields, (2) high nonlinearity, (3) strong confinement, and (4) low-loss interconnection to other optical fibers and fiberized components.[25] These facts open an even greater range of possibilities for the PCFs future applications.

MATERIALS AND METHODS

Materials. Sodium bis(2-ethylhexyl) sulfosuccinate (AOT, 99% Sigma), isooctane (Merck, MW = 114.23 g mol^{-1}, δ = 0.688 g cm^{-3}), *n*-heptane (Merck, MW = 100.21 g mol^{-1}, δ = 0.684 g cm^{-3}), *n*-hexane (Merck, MW = 86.18 g mol^{-1}, δ = 0.6548 g cm^{-3}), cyclohexane (Merck, MW = 84.16 g mol^{-1}, δ = 0.776 g cm^{-3}), and sodium tetraethyl orthosilicate (TEOS, Aldrich, 98%) were used without further purification. For microemulsion preparation, only triple-distilled water was used.

Materials Synthesis. Experiments were performed on water/AOT/alkane microemulsion systems. The composition of the microemulsion is given in terms of W_0, the ratio of water to surfactant molar concentrations, and S_0, the ratio of oil to surfactant molar concentration. Microemulsion systems of S_0 = 30 and W_0 = 60 were prepared using the injection method[26] by mixing an appropriate quantity of water with an AOT solution in oil. The resulting microemulsions were placed in Teflon-stoppered test tubes and aged for 24 h at 40 °C before used. Four microemulsion template systems were tested using isooctane, *n*-heptane, *n*-hexane, and cyclohexane as the oil phase. As the critical micellization concentration (CMC) of AOT[27] in both oil and water is low compared with the concentration used here, it can be presumed that all the surfactant molecules are localized at the interface between water and oil.

To obtain the SiO_2 materials, 11.6 mL of TEOS was dissolved in 2 mL of water and stirred for 10 min at 500 rpm. Then, a solution of 1.1 g of NaOH in 20 mL of water was added drop-by-drop to the TEOS solution while stirring. A minute later, the above-described microemulsion systems were poured into the mixture and stirred for 5 min. The resulting gels were left for 8, 15, and 24 h in an autoclave at 100 °C. The obtained materials were filtered, washed with triple-distilled water, and left to dry at room temperature. Finally, they were calcined for 7 h at various temperatures from 500 to 800 °C in an air flux.

Field Emission Scanning Electron Microscopy (FE-SEM). Field emission scanning electron microscopy (FE-SEM) was performed using a FESEM ULTRA PLUS. Resolution: 0.8 nm at 30 kV; accelerating voltage: 0.02 V−30 kV (continuously adjusted in steps of 10 V); magnification range 12−1000000×; sizes of openings: 7.5, 10, 20, 30, 60, and 120 μm. Local compensation of charge, by injecting nitrogen gas.

Transmission Electron Microscopy (TEM). Transmission electron microscopy was performed using a Philips CM-12 transmission electron microscope equipped with a digital camera MEGA VIEW-II DOCU and operated at 120 kV with magnification of 730000×. High-resolution transmission microphotographs were taken using a Libra 200 FE OMEGA transmission electron microscope operated at 200 kV with magnification of 1000000×. Observations were made in a bright field. Powdered samples were placed on cooper supports of 2000 mesh.

X-ray Powder Diffraction. Powder X-ray diffraction (XRD) data were collected with a Philips PW 1710 diffractometer with Cu Kα radiation (λ = 1.5418 nm) and graphite monochromator operated at 45 kV, 30 mA, and 25 °C.

FT-IR Spectroscopy. Infrared spectra were collected using a Varian 670 Fourier transform infrared spectrometer (FT-IR) equipped with a pneumatic motion interferometer. The spectra is a result of 100 accumulating scans measured peak to peak with a spectral resolution of 4 cm^{-1}. To avoid coadsorbed water, the samples were dried under vacuum until constant weight was achieved and diluted with KBr powder before the FT-IR spectra were recorded.

UV−vis and Fluorescence Spectroscopy. The UV−vis and fluorescence absorption spectrum was recorded at 298 K by a UV−vis−NIR scanning spectrophotometer (Beckman, model DU 640) and a Varian Cary Eclipse spectrofluorometer (under excitation by UV light at 220 nm), respectively, using a 1 cm path length quartz cell. The spectrum was obtained for the M1 and M2 materials that had been sonicated in ethanol to yield homogeneous dispersions. Pure ethanol solution was used as blank.

RESULTS AND DISCUSSION

Synthesis Conditions. In general, several factors should be considered carefully when selecting a suitable surfactant for a specific synthesis reaction in reverse micelles. Among the various surfactants exploited in formulating microemulsions for nanoparticle synthesis, we choose the anionic double-chained surfactant AOT because it can form reverse micelles without the need of cosurfactants.[16] Furthermore, irrespective of the nature of the apolar solvent, AOT molecules form nearly spherical and monodisperse water-containing reverse micelles, the size of which is quite dependent on the surfactant concentration and regulated mainly by W_0. For the nanoparticle synthesis we worked inside the AOT isotropic fluid phase L_2 where the structures of aggregates are only spheres.[28]

The dynamic nature of the reverse micelles plays a key role in the formation of the final nanoparticle morphology. This, in turn, is closely related to the rigidity of the nanodroplet oil−water interface.[16] Figure 1 shows the SEM microphotographs of the four different materials obtained by TEOS hydrolysis inside microemulsion droplets of different film rigidity (obtained by changing the oil template microemulsion phase), after hydrothermal treatment (100 °C, 24 h) and calcination (650 °C, 7 h) in air flux. Fibrils were obtained only when the oil phases used in the template microemulsion are *n*-hexane and cyclohexane. When isooctane or *n*-heptane was used as oil phase, a bicontinuous material was obtained. The film flexibility is increased by augmenting oil molecular weight (from cyclohexane to isooctane); contrary to what might be expected, the fiber structures are formed in those emulsions whose droplets have a more rigid film. That is, fibrils formation requires a certain stiffness in the oil−water interface.

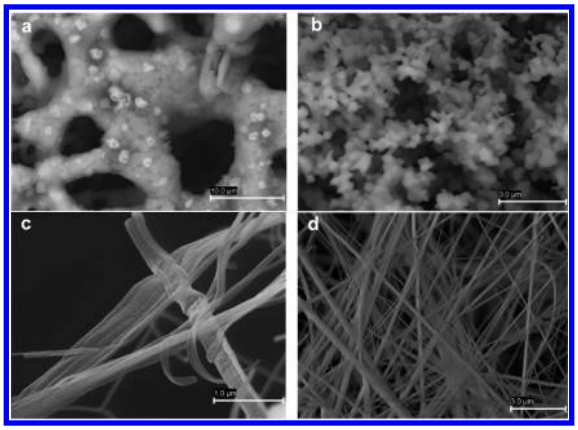

Figure 1. SEM microphotographs of SiO_2 materials templated with (a) water/AOT/isooctane, (b) water/AOT/*n*-heptane, (c) water/AOT/*n*-hexane, and (d) water/AOT/cyclohexane microemulsions.

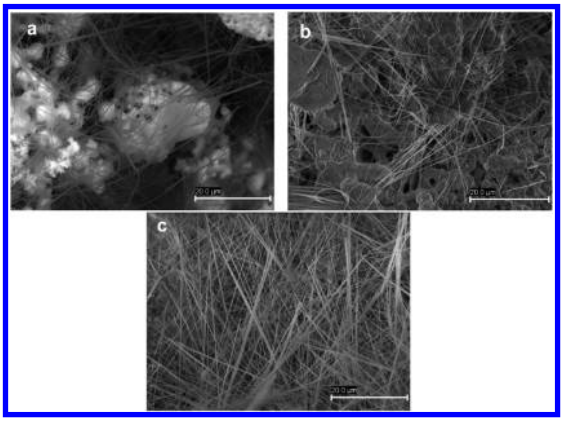

Figure 2. SEM microphotographs of SiO_2 materials obtained from water/AOT/cyclohexane template microemulsion after (a) 8 h, (b) 15 h, and (c) 24 h of hydrothermal treatment.

To explain this we must remember that in our case the syntesis is performed through a hydrothermal treatment. Essentially, there are two mechanisms proposed for the microemulsion-mediated synthesis of inorganic nanowires/nanorods: the template-directed growth and the oriented aggregations.[16,29] In the template-directed growth mechanism, elongated water droplets or interconnected water channels play the role of template to induce the formation of elongated nuclei, which finally grow into nanorods with dimensions considerably larger than the templates. In the oriented aggregation mechanism, precipitation within spherical water droplets initially results in the formation of surfactant-encapsulated primary nanoparticles which subsequently undergo oriented aggregation involving linear attachment and coalescence owing to specific interactions of inorganic crystals with surfactants leading to the growth of single-crystalline nanowires. Under hydrothermal conditions, an oriented aggregation mechanism is usually adopted because reverse micelles may be destroyed under synthesis conditions.[16] When the film is flexible (oil phase: isooctane, *n*-heptane), the resulting material presents a spongy structure denoting the formation of an interconnected water channels in the template microemulsion. By

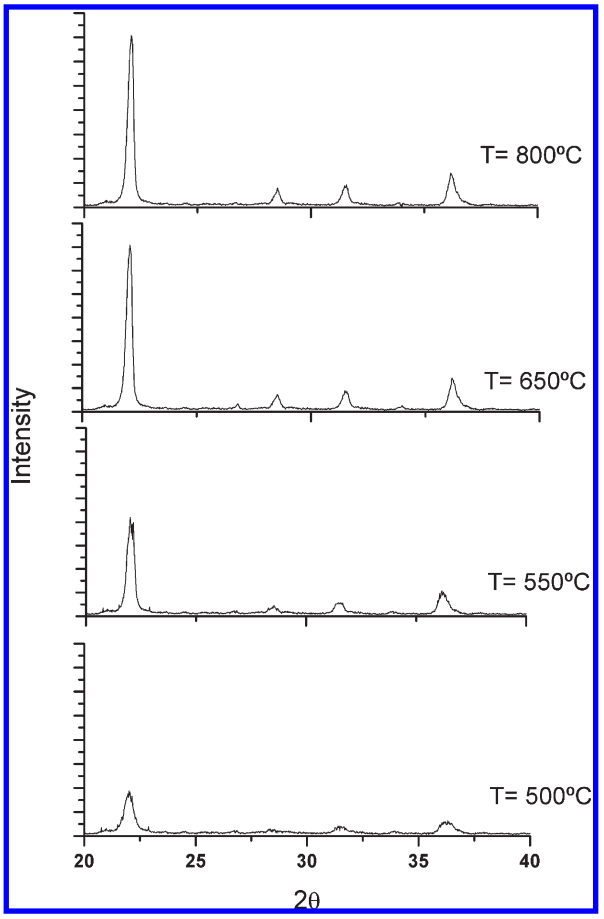

Figure 3. X-ray diffraction patterns of SiO_2 materials templated with water/AOT/hexane microemulsion calcined at 500, 550, 650, and 800 °C.

subjecting the microemulsion to the effects of hydrothermal treatment, reverse micelles are broken as shown in the oriented aggregation mechanism, and due to their flexible interface, the nanodroplets merge adopting a bicontinuous structure. When *n*-hexane and cyclohexane are used instead of isooctane or *n*-heptane, the nanodroplet films seems to be rigid enough to prevent the formation of interconnected channels.

At light of the obtained results, it was found that hydrothermal treatment is a crucial point in the synthesis of materials. Therefore, for those microemulsion systems giving rise to fibrils (water/AOT/*n*-hexane and water/AOT/cyclohexane), different times of treatment were tested. Figure 2 shows the SEM microphotographs of materials obtained from water/AOT/cyclohexane template microemulsion after 8, 15, and 24 h of hydrothermal treatment. It can be seen that the number of fibrils increases with the time of hydrothermal treatment, no differences in the material structure were seen after 24 h. Similar results were seen for the material templated with water/AOT/*n*-hexane (see Supporting Information).

Usually, the products obtained by alkoxide hydrolysis reverse micelles are amorphous or poorly crystallized, and subsequent calcinations are necessary for obtained the desired crystalline nanophase.[16,30,31] Figure 3 shows X-ray diffraction patterns (XRD) of M1 calcinated at 500, 550, 650, and 800 °C. The decrease in the full width at half-maximum (FWHM) of peaks

dx.doi.org/10.1021/la201555f |*Langmuir* 2011, 27, 8905–8912

Table 1. Final Synthesis Conditions of Fibrous Materials

material	microemulsion system	hydrothermal treatment	calcination conditions
M1	water/AOT/*n*-hexane	24 h, 100 °C	7 h, 650 °C
M2	water/AOT/cyclohexane	24 h, 100 °C	7 h, 650 °C

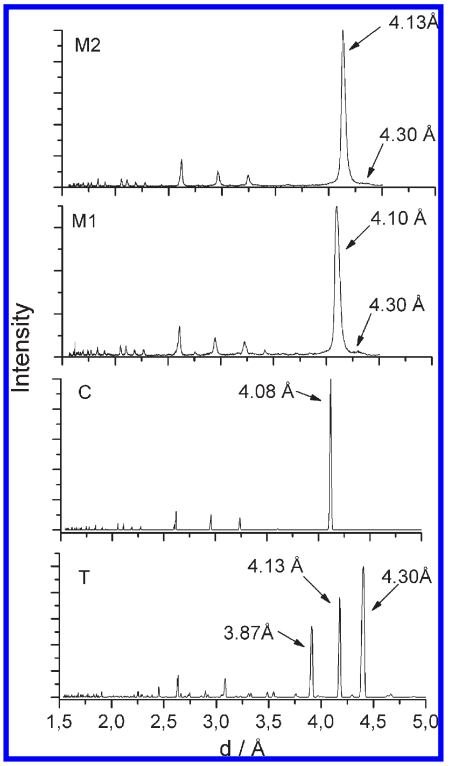

Figure 4. X-ray diffraction patterns of SiO_2 materials templated with water/AOT/hexane (M1) and water/AOT/cyclohexane (M2) microemulsions. C: α- cristobalite; T: α-tridymite.

with increasing temperature indicates an increase in the material crystallinity. No considerably differences were seen between the material calcined at 650 and 800 °C.

The synthetic conditions that resulted in unusual fibrous structure materials are summarized in Table 1. Their characterization is discussed below.

Material Characterization. Sample diffractograms were compared to the RRUFF database:[32] R061107.9 for α-cristobalite and R090042.9 for orthorhombic α-tridymite. Hydrous SiO_2 phases are widespread in volcanic sedimentary rocks associated with postvolcanic hydrothermal activity, devitrification, and diagenetic alteration. Opals are micro- and noncrystalline forms of hydrated silica with high degree of structural disorder.[33] On the basis of powder X-ray diffraction (XRD) data, Jones and Segnit[34] distinguished three hydrous silica phases at low temperatures: amorphous opal (opal-A), disordered cristobalite with significant tridymite stacking (opal-CT), and more ordered cristobalite with minor tridymite stacking (opal-C). Opal-CT and opal-C are considered as microcrystalline varieties of hydrous silica.

The two fibrous synthesized materials, M1 and M2, present the structure of opal-CT (Figure 4). They exhibit XRD patterns strongly resembling that of α-cristoballite with slight broadening

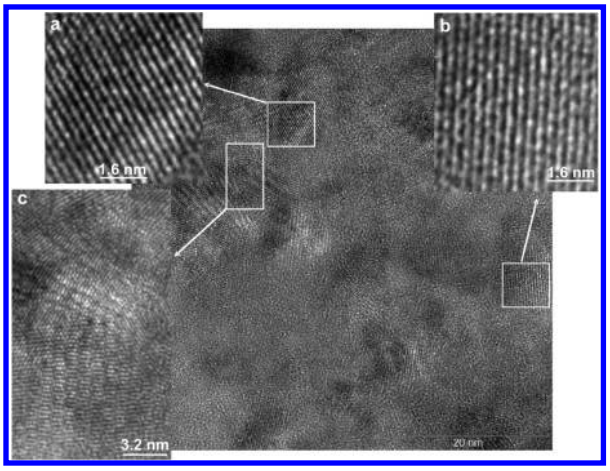

Figure 5. High-resolution TEM microphotograph of a single fiber section, showing the lattice planes. Cristobalite stacking (a, b) interrupted by several planar trydimite boundaries (c).

of the Bragg reflections, slight shift to larger *d*-spacings, and a weak extra peak near 4.30 Å—all which are characteristics of opal-CT and due to the presence of trydimite-type layers within the cristobalite structure. M2 exhibits a slight shift to larger *d*-spacing with respect to M1, which corresponds to a major abundance of tridymite-type stacking faults in the [111] direction of the cristobalite three-layered structure.[33] No peaks related to quartz ($2\theta = 26°$) or phyllosilicates ($2\theta = 6°$)[35] are identified (see Supporting Information).

Using transmission electron microscopy (TEM) and XRD, Elsea and Rice[36] concluded that the dominant phase in opal-CT samples was essentially α-cristobalite with a high degree of stacking disorder. Figure 5 shows the cristobalite stacking (a, b) interrupted by several planar tridymite boundaries (c) in M1 material; similar results were obtained for M2. The results are consistent with X-ray diffractions.

The FT-IR spectroscopic study performed on both samples show the characteristic peaks of α-cristobalite (1200 and 622 cm^{-1}) just with weak additional absorption bands at the 3700−3200 cm^{-1} range belonging with tridymite (see Supporting Information).

Opal-CT Microstructure. FE-SEM (Figure 1c,d) and TEM (Figure 6) microphotographs revealed an unusual fibrous arrangement. Both samples present a very similar microstructure; they are long fibrils of 30−50 nm diameter and greater than 20 μm length. These form bundles of 100−200 nm distributed in different orientations. Opals fibrils are made up of α-SiO_2 polyhedral spheres that are monodisperse in size ($d \approx 2$ Å) (Figure 7). They form, as usual, (111) hexagonal layers superimposed on one another along the [111] axis to form an fcc (face-centered-cubic) lattice.[37] Each layer perpendicular to the [111] direction is a triangular lattice with periodicity equal to sphere diameter, $d = a/\sqrt{2}$, where *a* is the fcc lattice constant, and it is shifted with respect to the previous one by a quantity equal to $d/\sqrt{3}$ as shown in Figure 7c; this is the so-called graphite layer arrangement.[38] A vertical cross section of the opal structure in the *yz* plane is shown Figure 7d. The distance between two planes of spheres d_{111} along the [111] direction is given by[38]

$$d_{111} = \sqrt{\frac{2}{3}}d = \frac{a}{\sqrt{3}} \quad (1)$$

dx.doi.org/10.1021/la201555f |*Langmuir* 2011, 27, 8905–8912

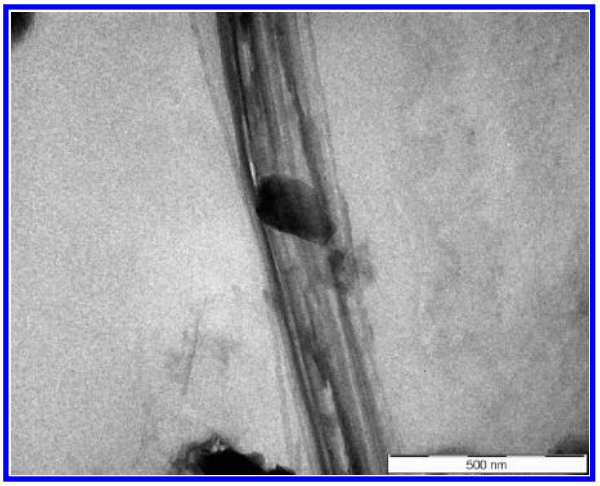

Figure 6. TEM microphotograph of M1 opal-CT fibrils.

The height H_{cap} of the sphere caps and their radius R_{cap}, also shown in Figure 7d, at the contact point between sphere caps are the following:[38]

$$H_{cap} = \left(1 - \sqrt{\frac{2}{3}}\right)d, \quad R_{cap} = \frac{d}{2\sqrt{3}} \qquad (2)$$

The lattice constant (a = 2.83 Å) is on the order of angstroms as for ordinary crystals as well as the computed values of d_{111} = 1.63 Å, H_{cap} = 0.37 Å, and R_{cap} = 0.58 Å. The fibrous microstructure of opals is remarkable and unusual; to our knowledge only some natural pink opals have this structure.[15] Natural fibrous opals may occur only in a very specific geological environment, and its fibrous microstructure is due to the presence of a phyllosilicate.[15] As we have confirmed the absence of phyllosilicates in the materials, it can be said that fibril microstructure is a consequence of the specific conditions of the microemulsion-hydrothermal mediated synthetic route. We believe that an oriented aggregation mechanism may be operative in our molecular sieve synthesis influenced by the film rigidity and that the final opal-CT microcrystalline structure was achieved after calcination.

It cannot be appreciate any significant effect on particle size by changing the oil phase in microemulsion template system; however, the changes of the oil phase from *n*-hexane to cyclohexane and the consequent increment of the film rigidity cause a change in the opals-CT microstructure. M1 fibrils appear to be somewhat more flexible than those of M2 in accordance with an increase in the film stiffness going from hexane to cyclohexane. Furthermore, the material synthesized by water/AOT/cyclohexane microemulsion (M2) presents a small increase of stacking disorder in the cristobalite layers. It is assumed that an increase of film stiffness hinders the TEOS hydrolysis and leads to a less tidy end product. This apparently minimum effect has a great influence in the material optical properties as shown below.

Optoelectronic Studies of Synthetic Opals. There are mainly two types of photoluminescence (PL) emission in Si nanostructures at room temperature. The yellow−orange−red PL bands with a slow decay of the order of μs to ms (the so-called "slow bands", abbreviated as the S-band) is usually dominant and receives the most attention, while the fast blue−green PL bands (the so-called F-band with a characteristic decay time on the order of ns) is observed and reported infrequently. The last ones are predominantly in rapidly oxidized porous silicon structures.[39]

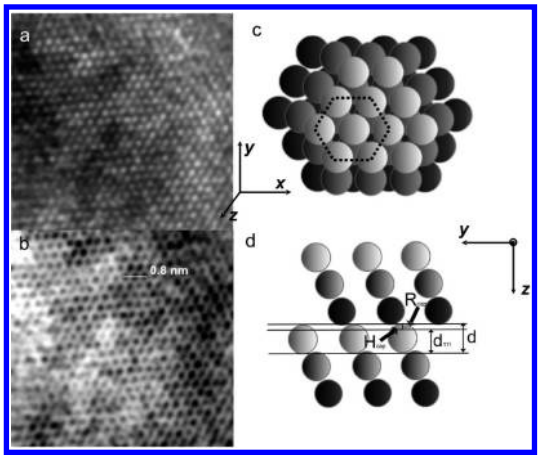

Figure 7. (a) High-resolution TEM microphotograph of a single fiber section, showing the close-packed fcc lattice. (b) For better viewing of the (a), the image colors were reversed. (c) Scheme of the close-packed fcc lattice seen from [111] direction; hexagonal face in dashed black line. (d) Cross-sectional view of an fcc lattice oriented along [111] direction; the region between two consecutive planes is defined by two straight lines.

Figures 8 and 9 show the photoluminescence (PL) emission spectra of M1 and M2 materials excited at 220 nm. Both samples exhibited largely Stokes-shifted (short wavelength) and band-edge (long wavelength) emissions that depend largely from their microestructure. M1 presents a high intensity ultraviolet A (UVA) PL while M2 emits ultraviolet A and B radiations. Also, both materials PL spectra show two peaks of much less intensity that correspond to visible radiation: orange and green PL for M1 and bright red and yellow PL for M2. The dissimilarities between emission spectra of the two samples confirm the fact that they have different morphological properties.

Besides the differences in PL decay time, the F- and S-bands have different spectral behavior. While the S-band has an almost stable position under different excitation wavelengths, the F-band peak is shifted with the excitation wavelength.[39] From the analysis of Figure 10, it can be seen that bands around 550−700 nm present an almost stable spectra location with the increment of excitation wavelength, while there is an increment of intensity. Nevertheless, those bands at 270−350 nm shifts toward fewer wavelengths with the augment of excitation energy. The intensity and form of spectral bands are also very different. So, we identify the first as S-bands and the seconds as F-bands. We think that different types of luminescence centers in the Si oxide layers with energy around 3.6−3.8 and 1.9−2.1 eV are responsible for the ultraviolet (F-bands) and visible light emissions (S-bands). The luminescence mechanism of siliceous materials is persistently a focus of research, and many models have been proposed;[40] but so far it is still not entirely understood. Some authors proposed that more than one type of mechanism were needed for interpret the PL from nanoscale Si/Si oxide systems. It was suggested that for the S (slow)-band luminescence the quantum confinement (QC) model[41] works. The F (fast)-band luminescence has been interpreted as a part of two districts mechanisms: (i) intrinsic optical recombination in ultrasmall Si nanoparticles, with strong quantum-confinement effect and a large bandgap opening,[42] or (ii) recombination in defective silicon oxide particles.[43] It is difficult to distinguish the correct model of the F-bands in a given Si nanostructure.[39]

dx.doi.org/10.1021/la201555f |*Langmuir* 2011, 27, 8905–8912

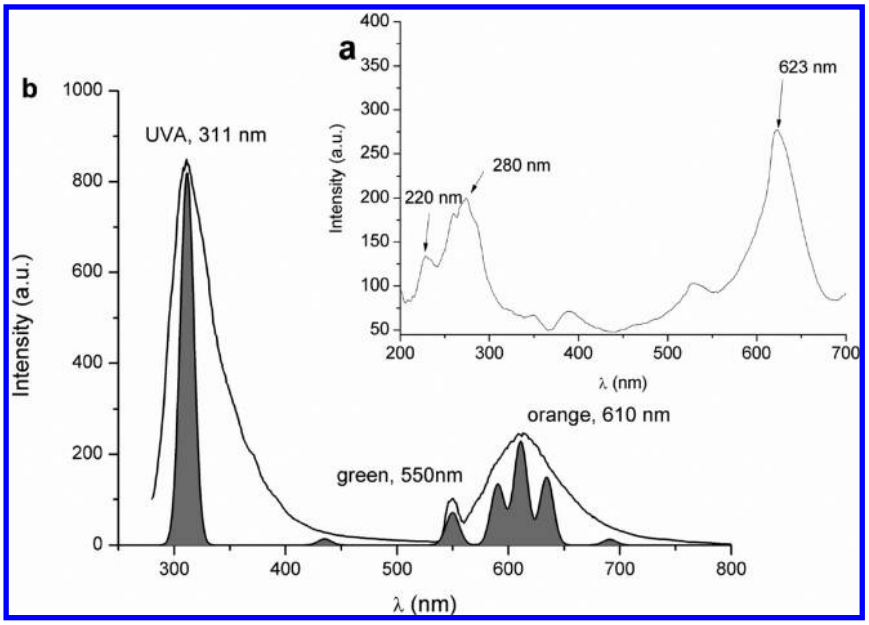

Figure 8. (a) Excitation and (b) PL spectra (λ = 220 nm) of M1. Relevant deconvolute peaks (shown in dark gray).

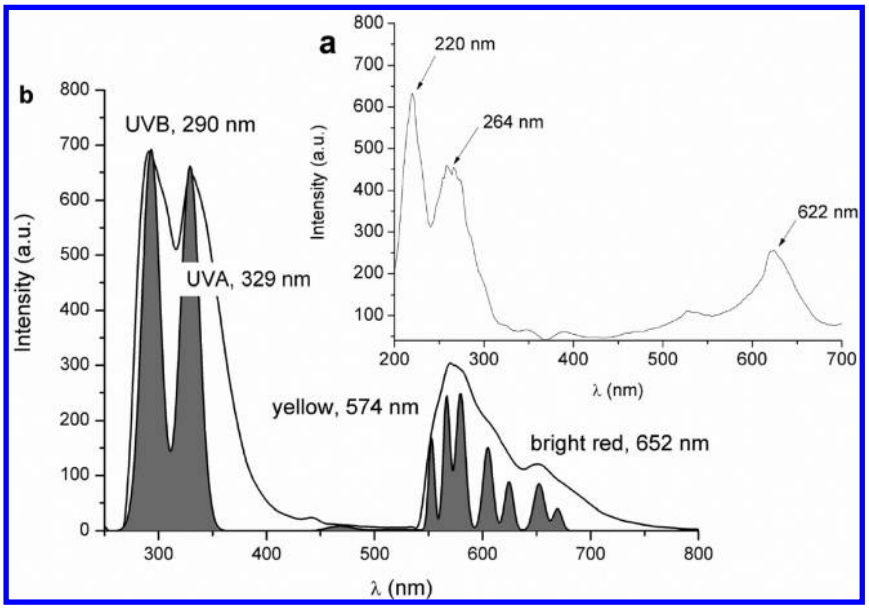

Figure 9. (a) Excitation and (b) PL spectra (λ = 220 nm) of M2. Relevant deconvolute peaks (shown in dark gray).

It was known that crystalline Si (c-Si) nanoparticles of sizes comparables to or smaller than the Si exciton Bohr radius in bulk (4.3 nm) show a quantum confinement effect resulting in an enhanced recombination of excitons. Therefore, the optical properties of c-Si nanoparticles and nanostructures are also sensitive to the surface geometry and chemistry.[44] On basis of these assumptions, we think that a combination of both mechanisms operate simultaneously in our materials and leads to orange−red luminescence (S-band luminescence) and blue−green and ultraviolet (F-band luminescence) components. In our materials, the F-bands (UV bands) are of greater intensity and different according to the material oxide layers distribution in the materials; consequently, we can assume that the predominant effect seems to be the distortion of the oxide layers on the quantum confinement. M2 with a high proportion of defective layer oxide surfaces shows two F-band emissions. In general, photoexited charge carriers (electron and hole) recombine with each other through several recombination processes such as direct band-to-band coupling and/or shallow/deeply trapped potential states.[45] Defect sites existing on the surface oxide layers provide deeply trapped potential states which induce such largely Stokes-shifted emissions.[45] The intensity change of the largely Stokes-shifted emission is believed to be due to the surface density change of defective emission states,[46] and in our materials this density change of surface defect states come from the different array of oxide layers in the material microcrystalline structures.

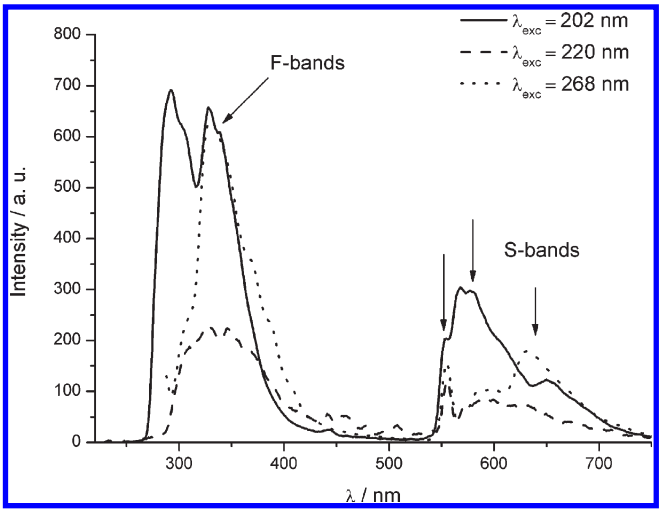

Figure 10. Photoluminescence spectra of M2 excited at different wavelengths.

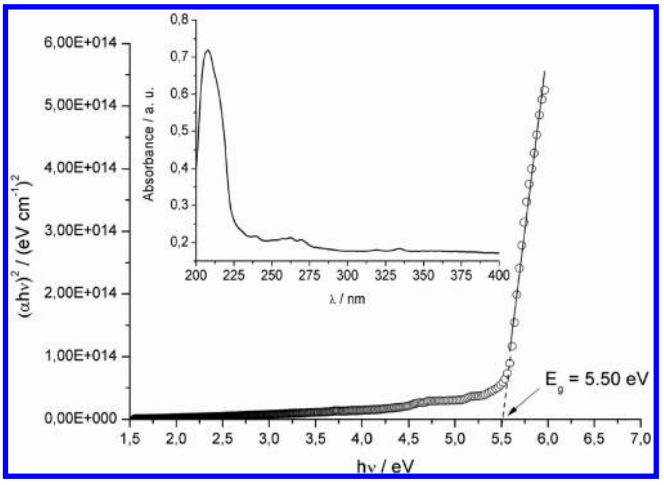

Figure 11. Estimation of band gap energy by plotting $(\alpha h\nu)^2$ vs $h\nu$. Inset: M1 absorption spectrum.

The band gap energy was estimated by plotting $(\alpha h\nu)^m$ of the microcrystalline opals against the photon energy $(h\nu)$, as shown in Figure 11 where α is the absorption coefficient, $h\nu$ is the photon energy, and E_g is the band gap energy. We assume that the transition of electrons through the forbidden zone occurs between states corresponding to the maximum of the gap and the valence band minimum conductance, taking into account only direct transitions $m = 2$. The adsorption (A) is converted to the absorption coefficient using the following relationship:[47] $\alpha = (2.303 \times 10^3/lc)A\rho$, where A is the adsorption of the sample, ρ is the density of crystobalite (2.33 g cm^{-3}), l is the cuvette length (1 cm), and c is the concentration of the sample (c_{M1} = 0.001 g cm^{-3} and $c_{M2} = 2.1 \times 10^{-4}$ g cm^{-3}). The band gap energy was determined by extrapolating the adsorption coefficient (α) to zero. The computed band gap values ($E_{g,M1}$ = 5.50 eV and $E_{g,M2}$ = 4.41 eV) are highly inferior to the experimental band gap values obtained for SiO_2 polymorphs (8.9 eV for α-quartz and superior values for β-quartz, α-cristobalite, β-cristobalite, and tridymite[48]) and similar to those obtained for silicon-based metal oxide semiconductors (MOS).[49,50]

CONCLUSIONS

In the above study, we have designed a simple and controllable route for the synthesis of opals-CT materials with unusual fibrous microstructure similar to those existed in the nature using a bottom-up microemulsion droplet system as chemical microreactor. The microcrystalline structure of opals and consequently their optoelectronic properties are a result of a particular combination of all the relevant microemulsion parameter, hydrothermal treatment time, and calcination temperature.

The obtained fibrils are longer than 20 μm with a diameter of 30−50 nm and are clustered forming bundles of 100−200 nm distributed in different orientations. Fibrils are composed by α-SiO_2 polyhedral spheres that are monodisperse in size ($d \approx 2$ Å) packed, as usual in photonic crystals, in (111) hexagonal layers superimposed on one another along the [111] axis to form a 3D fcc lattice. The lattice constant (a = 2.83 Å) is on the order of angstroms as for ordinary crystals and very inferior to those obtained until now for synthetic opals. Because of their unusual microstructure, they exhibited short and long wavelengh photolumiscence emissions which differ according to the crystobalite−trydimite stacking. The material with high content of trydimite-type stacking faults shows high intensity ultraviolet A and B just with minor intensity bright-red and yellow emission, while the material that presents a high ordered script of cristobalite emits ultraviolet A, orange, and green light radiations. It is believed that a combination of a quantum mechanism and the presence of defective Si oxide layers are the responsible for the simultaneous emissions of S- and F-bands.

Additionally, the computed band gap values (5.50 and 4.41 eV) for both synthesized materials are similar to those obtained for silicon-based metal oxide semiconductors and highly inferior to the experimental band gap values obtained for pure crystalline SiO_2 polymorphs (8.9 eV).

ASSOCIATED CONTENT

Supporting Information. Characterization of M1 and M2 materials by DRX patterns, d-spacing, FT-IR spectra, and SEM microphotographs. This material is available free of charge via the Internet at http://pubs.acs.org.

AUTHOR INFORMATION

Corresponding Author

*Tel: +54 291 4595159. Fax: +54 291 4595160. E-mail: pmessina@uns.edu.ar.

ACKNOWLEDGMENT

The authors acknowledge Universidad Nacional del Sur (PGI 24/ZQ07), Concejo Nacional de Investigaciones Científicas y Técnicas de la República Argentina (CONICET, PIP-11220100100072.), Xunta de Galicia (Project No. PXI20615PN), and Education Audiovisual Culture, Executive Agency European Commission (EMUNDUS18) for their financial support. V.V. has a postdoctoral fellowship of CONICET. P.M. is an adjunct researcher of CONICET.

REFERENCES

(1) Hansen, K. P.; Iman, H. *Optik Photonik.* **2010**, *2*, 37–41.
(2) Alivisatos, P. *Nature Biotechnol.* **2004**, *22* (1), 47–52.
(3) Zhu, J.; Peng, H.; Connor, S. T.; Cui, Y. *Small* **2009**, *5* (4), 437–439.

(4) Gordon, R.; Sinton, D.; Kavanagh, K. L.; Brolo, A. G. *Acc. Chem. Res.* **2008**, *4* (8), 1049–1057.
(5) Blanco, A.; Chomski, E.; Grabtchak, S.; Ibisate, M.; John, S.; Leonard, S. W.; Lopez, C.; Meseguer, F.; Miguez, H.; Mondia, J. P.; Ozin, G. A.; Toader, O.; van Driel, H. M. *Nature* **2000**, *405*, 437–440.
(6) Vlasov, Y. A.; Bo, X.-Z.; Sturm, J. C.; Norris, D. J. *Nature* **2001**, *414*, 289–293.
(7) Rogach, A. L.; Kotov, N. A.; Koktysh, D. S.; Ostrander, J. W.; Ragoisha, G. A. *Chem. Mater.* **2000**, *12*, 2721–2726.
(8) Nebel, C. E. *Nature Photonics* **2009**, *3*, 564–566.
(9) Badding, J. V.; Copalan, V.; Sazia, P. *Photonic Spectra* **2006**, 1–6.
(10) Gorelik, V. S.; Zlobina, L. I.; Troitskii, O. A.; Chanieva, R. I. *Inorg. Mater.* **2009**, *45* (7), 785–790 and references therein.
(11) Kirchhof, J.; Kobelke, F.; Schuster, K.; Barteli, H.; Iliew, R.; Etrich, C.; Ledere, F. Photonic crystal fibers. In *Photonic Crystals: Advances in Design, Fabrication and Characterization*; Busch, K., Lölkes, S., Wehrspohn, R. B., Föll, H., Eds.; Wiley-VCH Verlag GmbH & Co.: Weinheim, 2004; pp 266−286.
(12) Russell, P. *Science* **2003**, *299*, 358–362 and references therein.
(13) Astratov, V. N.; Bogomolov, V. N.; Kaplyanskii, A. A.; Prokofiev, A. V.; Samoilovich, L. A.; Samoilovich, S. M.; Vlasov, Y. A. *Nuovo Cimento Soc. Ital. Fis., D* **1995**, *17*, 1349–1354.
(14) Sakoda, K. In *Optical Properties of Photonic Crystals*; Springer-Verlag: Berlin, 2005.
(15) Fritsch, E.; Gaillou, E.; Ostroumov, M.; Rondeau, B.; Devouard, B.; Barreau, A. *Eur. J. Mineral.* **2004**, *16*, 743–752.
(16) Qi, L. *Encycl. Surf. Colloidal Sci.* **2006**, 6183–6207 and references therein.
(17) Pinna, N.; Wild, U.; Urban, J.; Schlögl, R. *Adv. Mater.* **2003**, *15*, 329–331.
(18) Kaneko, D.; Shouji, H.; Kawai, T.; Kon-No, K. *Langmuir* **2000**, *16*, 4086–4089.
(19) Zhang, P.; Gao, L. *Langmuir* **2003**, *125*, 208–210.
(20) Cao, M. H.; Hu, C. W.; Wang, E. B. *J. Am. Chem. Soc.* **2003**, *125* (11), 196–197.
(21) Zhang, D. F.; Sun, L. D.; Yin, J. L.; Yan, C. H. *Adv. Mater.* **2003**, *15*, 1022–1025.
(22) Yates, M. Z.; Ott, K. C.; Birnbaum, E. R.; McCleskey, T. M. *Angew. Chem., Int. Ed.* **2002**, *41*, 476–478.
(23) Lin, J. C.; Diere, J. T.; Yates, M. Z. *Chem. Mater.* **2003**, *15*, 2764–2773.
(24) Cao, M. H.; Wang, Y. H.; Guo, C. X.; Qi, Y. J.; Hu, C. W. *Langmuir* **2004**, *20*, 4784–4786.
(25) Brambilla, G.; Xu, F.; Horak, P.; Jung, Y.; Koizumi, F.; Sessions, N. P.; Koukharenko, E.; Feng, X.; Murugan, G. S.; Willkinson, J. S.; Richardson, D. J. *Adv. Inf. Opt. Photonics* **2009**, *1*, 107–161.
(26) Alexandridis, P.; Holzwarth, J. F.; Hatton, T. A. *Langmuir* **1993**, *9*, 2045–2052.
(27) Moha-Ouchane, M.; Peyrelasse, J.; Boned, C. *Phys. Rev. A* **1987**, *35*, 3027–3032.
(28) Alexandridis, P.; Holzwarth, J. F.; Hatton, T. A. *J. Phys. Chem.* **1995**, *99*, 8222–8232 and references therein.
(29) Qi, L. *Coord. Chem. Rev.* **2010**, *254*, 1054–1071.
(30) Hung, I.-M.; Hung, D.-T.; Fung, K.-Z.; Hon, M.-H. *J. Eur. Ceramic Soc.* **2006**, *26*, 2627–2632.
(31) Chen, S.-Y.; Tang, C.-Y.; Lee, J.-F.; Jang, L.-Y.; Tatsumi, T.; Cheng, S. *J. Mater. Chem.* **2011**, *21*, 2255–2265.
(32) http://rruff.info/.
(33) Ilieva, A.; Mihailova, B.; Tsintsov, Z.; Petrov, O. *Am. Mineral.* **2007**, *92*, 1325–1333.
(34) Jones, J. B.; Segnit, I. R. *J. Geol. Soc. Aust.* **1971**, *18*, 57–68.
(35) Ghisoli, C. *Sci. Acta* **2008**, *2*, 27–34.
(36) Elzea, J. M.; Rice, S. B. *Clays Clay Miner.* **1996**, *44*, 492–500.
(37) Baryshev, A. V.; Kaplyanskii, A. A.; Kosobukin, V. A.; Samusev, K. B.; Usvyat, D. E.; Limonov, M. F. *Phys. Rev. B* **2004**, *70*, 1131041.
(38) Grosso, G.; Pastori Parravicini, G. *Solid State Physics*; Academic Press: New York, 2000.
(39) Valenta, J.; Fucikova, A.; Pelant, I.; Kůsová, K.; Dohnalová, K.; Aleknavičius, A.; Cibulka, O.; Fojtík, K. G. *New J. Phys.* **2008**, *10*, 073022 and references therein.
(40) Qin, G. G.; Li, Y. J. *Phys. Rev. B* **2003**, *68*, 085309 and references therein.
(41) Qin, G. G.; Jia, Y. Q. *Solid State Commun.* **1993**, *86*, 559–563.
(42) Kanemitsu, Y. *J. Lumin.* **2002**, *100*, 209–214.
(43) Švrček, V.; Sasaki, T.; Shimizu, Y.; Koshizaki, N. *Appl. Phys. Lett.* **2006**, *89*, 213113.
(44) Komuro, S.; Kato, T.; Morikawa, T.; ÓKeeffe, P.; Aoyagi, Y. *J. Appl. Phys.* **1996**, *80*, 1749.
(45) Gaponenko, S. V. *Optical Properties of Semiconductor Nanocrystals*; Cambridge University Press: New York, 1998.
(46) Chang, C. L.; Fogler, H. S. *Langmuir* **1997**, *13*, 3295–3307.
(47) Serpone, N.; Lawless, D.; Khairutdinov, R. *J. Phys. Chem.* **1995**, *99*, 16646–16654.
(48) Gnani, E.; Reggiani, S.; Colle, R.; Rudan, M. *VLSI Design* **2001**, *13* (1−4), 311–315.
(49) Yamasaki, T.; Kaneta, C.; Uchiyama, T.; Uda, T.; Terakura, K. *Phys. Rev. B* **2001**, *63*, 1153141–1153145.
(50) Städale, M.; Tuttle, B.; Fischer, B.; Hess, K. *J. Comput. Electron.* **2002**, *1*, 153–159.